PAPER

CrossMark
click for updates

Incorporation of square-planar Pd^{2+} in fluorite CeO_2: hydrothermal preparation, local structure, redox properties and stability†

Craig I. Hiley,[a] Janet M. Fisher,[b] David Thompsett,[b] Reza J. Kashtiban,[c] Jeremy Sloan[c] and Richard I. Walton*[a]

The direct hydrothermal crystallisation at 240 °C of Pd^{2+}-containing ceria is investigated to study the extent to which precious metal dopants may be introduced into the cubic fluorite lattice. Samples of composition $Ce_{1-x}Pd_xO_{2-\delta}$, where $0 \leq x \leq 0.15$ can be produced in which Pd is included within the CeO_2 structure to give a linear lattice expansion. Attempts to produce higher Pd^{2+}-substitution result in the formation of PdO as a secondary phase. Ce and Pd were determined to be in the +4 and +2 oxidation states, respectively, by X-ray absorption near edge structure, suggesting oxide deficiency as the mechanism of charge balance. Extended X-ray absorption fine structure (EXAFS) analysis at the Pd K-edge reveals that Pd^{2+} has local square-planar coordination, as expected, and that a structural model can fitted in which the average fluorite structure is maintained, but with Pd^{2+} sitting in the square faces of oxide ions present in the local cubic geometry of Ce. This model, consistent with previous modelling studies, gives an excellent fit to the EXAFS spectra, and explains the observed lattice expansion. Transmission electron microscopy analysis shows that Pd is well dispersed in the nanocrystalline ceria particles, and *in situ* powder XRD shows that upon heating in air the samples remain stable up to 800 °C. H_2-TPR shows that Pd-substitution leads to low temperature (<200 °C) reduction of the oxide, which increases in magnitude with increasing Pd-substitution. On prolonged heating, however, the Pd is lost from the ceria lattice to give dispersed Pd metal, suggesting an inherent instability of Pd-doped CeO_2.

Introduction

Cerium dioxide (ceria) and doped variants are well known to be an essential component of a range of important heterogeneous catalyst systems of relevance to energy and the environment.[1,2] The ability of ceria to release oxygen whilst maintaining the average fluorite structure (consisting of a cubic close packed array of Ce^{4+} ions with oxide ions occupying the tetrahedral sites) and readily re-oxidise in oxidising conditions makes it an ideal oxygen buffer. This is facilitated by high oxide mobility in the fluorite structure and the Ce^{4+}/Ce^{3+} redox couple at moderate temperatures.[3] A small amount of precious metal, such as Rh, Pd or Pt, highly dispersed on the surface of ceria greatly improves its low temperature reducibility,[4,5] a feature much exploited for applications such as the water gas shift reactions[2,6,7] and automobile three-way catalysts.[5,6,8,9] Recent

work has also shown other catalysis applications for precious-metals/ceria, such as in the methane oxidation reaction.[10] Since this enhancement of properties, involving intimate, atomic-scale interaction, is widely considered to be a cooperative effect between the cerium oxide and the precious metal,[11] incorporation of precious metal ions into the ceria lattice may be considered as an atomic efficient alternative to surface immobilisation of precious metals.[12]

Substitution of isovalent[9,13] or aliovalent[14] metal ions into ceria is well known to improve oxide mobility as a result of lattice distortion and/or the formation of charge-compensating oxide vacancies.[15] The group of Hegde has been very successful in incorporating small amounts (≤5 mol% replacement of Ce) of precious metal into ceria, principally by a solution combustion method.[16] The materials $Ce_{1-x}M_xO_{2-\delta}$, (M = Pt, Pd, Rh, Ru) prepared *via* this route have shown favourable CO oxidation and NO reduction activity compared to the precious metal dispersed on the surface of CeO_2.[17–19] More recently, milder synthetic routes to preparing phase-pure $Ce_{1-x}Pd_xO_{2-\delta}$ with a higher degree of Pd substitution have been explored, such as ultrasonication,[20] ultrasonic spray pyrolysis[21] (x up to 0.10 in both cases) and coprecipitation of a microemulsion (x up to 0.21).[22] One report of hydrothermal preparation of precious metal-substituted ceria ($Ce_{0.95}Ru_{0.05}O_{2-\delta}$ and $Ce_{0.90}Ru_{0.10}O_{2-\delta}$) has

[a]*Department of Chemistry, University of Warwick, Gibbet Hill Road, Coventry, CV4 7AL UK. E-mail: r.i.walton@warwick.ac.uk*

[b]*Johnson Matthey Technology Centre, Sonning Common, Reading, RG4 9NH, UK*

[c]*Department of Physics, University of Warwick, Gibbet Hill Road, Coventry, CV4 7AL UK*

Fig. 1 The CeO$_2$ structure (two unit cells shown) with one Ce^{4+} ion substituted for by a Pd^{2+} ion. Pd^{2+} is shown in red, Ce^{4+} in dark blue and O^{2-} in orange. The resulting under-coordinated O^{2-} sites are shown in yellow. This under-coordinated site is 75% occupied to achieve charge-balance.

emerged,[23] despite the wide range of other metals ions substituted into ceria by this route.[24]

The oxidation state of Pd when included in ceria has been demonstrated to be +2 by X-ray absorption near edge spectroscopy (XANES)[18] and X-ray photoelectron spectroscopy (XPS).[18–20,25] Although a square-planar geometry is expected for Pd^{2+} with its 4d^8 electron configuration, existing extended X-ray absorption fine structure (EXAFS) studies[18,19] have failed to explain how a square-planar ion is accommodated into the fluorite structure. Scanlon *et al.* used density functional theory analysis[26] to show computationally that a Pd^{2+} dopant ion moved off the Ce site by 1/4 of a unit cell in one direction (~1.2 Å) to sit on the face of an oxide cube rather than the centre, is an energetically stable configuration (Fig. 1). In this model Ce^{4+} is replaced by Pd^{2+} so to balance charge oxide vacancies must also be present, and one of the oxygens becomes under-coordinated. To our knowledge, such a model has not been tested with any experimental data. In this paper we explore the hydrothermal synthesis of nanocrystalline Ce$_{1-x}$Pd$_x$O$_{2-\delta}$ ($0 \leq x \leq 0.25$) and examine the local chemical environment of Pd using EXAFS analysis before studying the stability of these materials in air and their redox properties in a reducing gas stream. Our aim was to explore the level of Pd incorporation possible in the CeO$_2$ structure by this soft chemical route and to examine the structural chemistry of the resulting phases, something not resolved satisfactorily in the literature at present. At the same time we have examined redox properties and stability.

Results and discussion

Structure and solubility limit

Powder XRD patterns of Ce$_{1-x}$Pd$_x$O$_{2-\delta}$ (Fig. 2a) show a single nanocrystalline fluorite phase is present in each case up to $x = 0.25$. When $x \geq 0.30$, Bragg peaks attributed to crystalline PdO were seen in the diffraction pattern. Whilst there is no indication of PdO in Ce$_{0.75}$Pd$_{0.25}$O$_{2-\delta}$ in the diffraction data, the lattice parameter is almost identical to that of Ce$_{0.80}$Pd$_{0.20}$O$_{2-\delta}$, suggesting that no more Pd has been substituted into the lattice by

this point. In fact a linear lattice expansion can be seen only up to $x = 0.15$ (Fig. 2b), suggesting the upper limit of Pd inclusion is actually between 0.15 and 0.20 (the EXAFS analysis described below clarifies this point). Other Pd-containing ceria samples reported in the literature have also been shown to exhibit lattice expansion with increasing Pd content: for example, Kurnatowska *et al.* produced materials by a water-in-oil microemulsion method followed by calcination in air at 500 °C and found a similar lattice expansion with homogeneous materials up to $x = 0.20$,[22] while Misch *et al.* produced materials with up to 10 mol% Pd substitution by ultrasonic spray pyrolysis at 500 °C, and also found a lattice parameter expansion,[21] although somewhat smaller than seen for our materials. Materials prepared by ultrasonication also show a maximum value of x of 0.10,[20] and the lattice parameters reported are
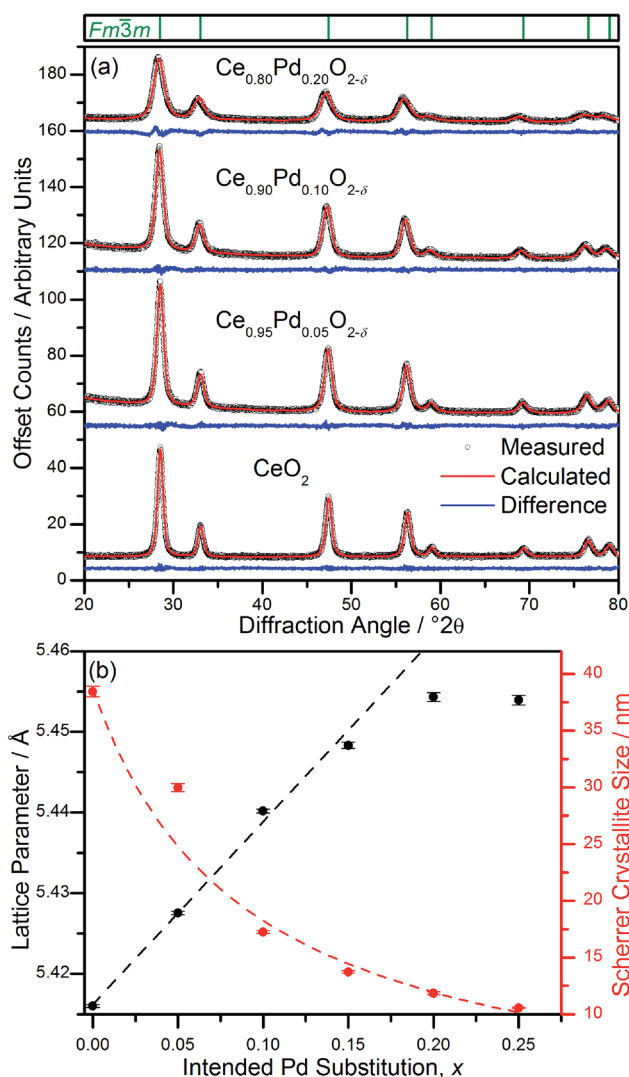

Fig. 2 (a) Fits to powder XRD data ($\lambda = 1.54056$ Å) of Ce$_{1-x}$Pd$_x$O$_{2-\delta}$ ($x = 0$, 0.05, 0.10, 0.20). Tick marks above denote positions of fluorite cell, space group $Fm\bar{3}m$. (b) Refined lattice parameter, a, and crystallite size as a function of intended Pd substitution, x. In (b) the linear fit of lattice parameters is over the range $0 \leq x \leq 0.15$ (see text for discussion) and the curved line is a guide to the eye.

Fig. 3 HR-TEM micrographs of (a) CeO_2, (b) $Ce_{0.90}Pd_{0.10}O_{2-\delta}$ and (c) $Ce_{0.80}Pd_{0.20}O_{2-\delta}$.

comparable to that of Misch *et al.* (see ESI Fig. S1† for a comparison between our materials and these literature values). Other published papers on Pd doping of ceria use much lower Pd content and lattice parameters are very similar to that of undoped CeO_2,[18,27] or are co-doped with other metals.[25,28]

The ionic radius of Pd^{2+} is significantly smaller (0.64–0.86 Å depending on geometry[29]) than eight-coordinate Ce^{4+} (0.97 Å (ref. 29)), and a lattice contraction would thus be expected if Pd were simply occupying the Ce 4a crystallographic site in the fluorite structure. The lattice expansion

observed is, however, consistent with the Pd^{2+} ion residing in a square-planar site at the centre of one of the faces belonging to the CeO_8 cubes, Fig. 1. An unexpanded fluorite CeO_2 unit cell would give Pd–O distances of ~1.91 Å in this arrangement, significantly shorter than has been found in other square-planar Pd oxides; such as PdO[30] and $La_2Pd_2O_5$ and La_4PdO_7,[31] all of which have Pd–O bond lengths of 2.01–2.07 Å. Thus the presence of Pd^{2+} in this environment would be expected to cause an expansion of the ceria lattice to accommodate the Pd^{2+} ion and give physically reasonable Pd–O

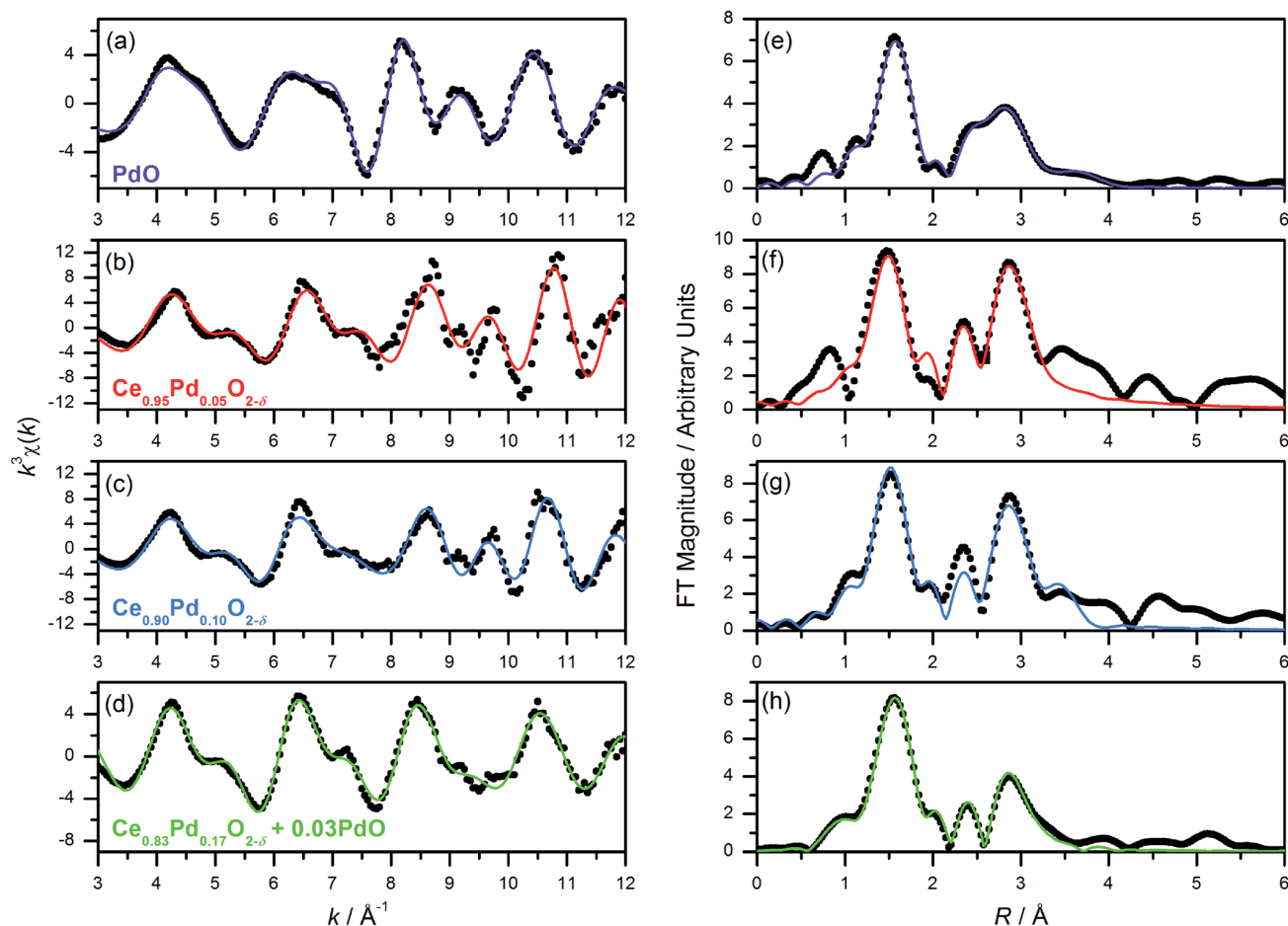**Fig. 4** (a–d) Pd K-edge k^3-weighted EXAFS spectra (points) with fits (lines); and (e–h) Fourier transforms of PdO, $Ce_{0.95}Pd_{0.05}O_{2-\delta}$, $Ce_{0.90}Pd_{0.10}O_{2-\delta}$ and $Ce_{0.80}Pd_{0.20}O_{2-\delta}$ (nominal composition), respectively.

bond lengths. The powder XRD also shows that there is significant broadening of the Bragg peaks as x is increased, suggesting that the crystallite size is decreasing. This effect has also been seen with other dopants in CeO_2.[32] It is also possible that strain associated with the distorted metal environment is a factor in peak broadening. Rietveld analysis of the structure is complicated by the broad diffraction profile and the likely high thermal parameters of oxygen, but using a model based on Fig. 1 the refined oxygen content is consistent with increasing oxide deficiency with increased Pd content and the general chemical formula $Ce_{1-x}Pd_xO_{2-\delta}$ (see ESI†).

Elemental analysis showed that the Ce : Pd ratio in the as-made oxides is the same as expected in the reaction mixtures (ESI, Table S1†). High resolution transmission electron microscopy of hydrothermally prepared CeO_2, $Ce_{0.90}Pd_{0.10}O_{2-\delta}$ and $Ce_{0.80}Pd_{0.20}O_{2-\delta}$ (Fig. 3) shows that the particle size decreases as x increases from around 10–20 nm of CeO_2 to sub-10 nm particles of $Ce_{0.80}Pd_{0.20}O_{2-\delta}$. Energy-dispersive X-ray spectroscopy (EDX) elemental analysis of $Ce_{0.90}Pd_{0.10}O_{2-\delta}$ and $Ce_{0.80}Pd_{0.20}O_{2-\delta}$ at multiple points found that the Ce : Pd ratio is both consistent with the intended values and the metals are homogeneously distributed throughout the oxides (ESI, Table S2†). Ce L_{III}-edge XANES spectra of all the samples (ESI, Fig. S3†) shows that the average Ce oxidation state and local environment remains as in CeO_2. While the presence of Ce(III) could also lead to lattice expansion, and indeed in small particles of CeO_2 some reduction of the cerium is often found,[33] for our materials there is no evolution of the XANES signal with Pd doping, so the increased Pd content must be largely be responsible for the lattice expansion. The Pd K-edge XANES suggests that the Pd is found primarily in the +2 oxidation state, although there is possible evidence for some local oxide deficiency giving partially oxidised Pd, since the local structure is not identical to as seen in PdO (ESI, Fig. S4†).

EXAFS analysis of local structure of Pd

Pd K-edge EXAFS spectra of $Ce_{1-x}Pd_xO_{2-\delta}$ ($x = 0.05$, 0.10, 0.20) show a marked difference to the spectrum of PdO (Fig. 4). The calculated $\chi(k)$ of PdO based on its crystal structure with distances and thermal parameters allowed to refine, fits closely the measured data (Fig. 4a, and Table 1), and this same model yields a poor fit to the Pd-substituted ceria fluorites with incorrect refined correlation distances and unphysical thermal parameters, eliminating the possibility of Pd existing solely as amorphous PdO in the ceria materials. We note here that previous EXAFS studies of Pd-doped ceria materials by Hegde and co-workers, erroneously assigned an O–O distance of 2.67 Å in PdO as due to Pd–Pd and used this in their EXAFS modelling,[18,34] so we are unsure as to the validity of their fitted parameters in the lightly doped samples they prepared by solution combustion. Instead we have used the structural model shown in Fig. 1 to describe the local structure, where Pd is substituted into ceria, but rather than occupying the Ce site it is shifted to sit at the centre of a plane of four equidistant O atoms. An initial model with no expansion of the unit cell was used (i.e. with Pd–O distances of 1.9 Å) and on refinement of structural parameters against the Pd K-edge EXAFS spectra of $Ce_{0.95}Pd_{0.05}O_{2-\delta}$, $Ce_{0.90}Pd_{0.10}O_{2-\delta}$ and $Ce_{0.80}Pd_{0.20}O_{2-\delta}$ (Fig. 4) increased correlation distances compared to the unexpanded model were produced, (Table 1) in accordance with the lattice expansion seen by powder XRD data, Fig. 2a. $Ce_{0.95}Pd_{0.05}O_{2-\delta}$ and $Ce_{0.90}Pd_{0.10}O_{2-\delta}$ can be well fitted by three shells of atoms and adding subsequent shells gave no improvement on the fit and caused the closer shells to have physically unreasonable values, suggesting a degree of disorder on this length scale. The fit to $Ce_{0.95}Pd_{0.05}O_{2-\delta}$ has a comparatively large R-factor due to the reduced signal-to-noise ratio, particularly evident at high k, in this dilute sample.

The Pd K-edge EXAFS signal of $Ce_{0.80}Pd_{0.20}O_{2-\delta}$ cannot be satisfactorily fitted solely by the same model, however. Since

Table 1 Pd K-edge EXAFS fitting results for crystalline PdO and $Ce_{1-x}Pd_xO_{2-\delta}$, ($x = 0.05$, 0.10, 0.20). R_{cryst} are expected crystallographic distances (see text for references) from the crystal structure of Waser et al. for PdO[30] or from the Model in Fig. 1

Compound (fit parameters)	Shell	Coordination number	R_{cryst}/Å	R/Å	σ^2/Å²
PdO ($S_0^2 = 0.826$, $E_0 = 1.052$ eV, R-factor $= 0.0312$)	O	4	2.018	2.035(10)	0.002(1)
	Pd	4	3.030	3.055(12)	0.008(1)
	Pd	8	3.420	3.482(48)	0.016(5)
	O	8	3.640	3.888(80)	0.010(12)
	O	4	4.275	4.319(82)	0.004(8)
	Pd	4	4.285	4.285(257)	0.023(40)
$Ce_{0.95}Pd_{0.05}O_{2-\delta}$, ($S_0^2 = 0.909$, $E_0 = -7.56$ eV, R-factor $= 0.179$)	O	4	1.910	1.963(26)	0.0022(37)
	Ce	4	3.030	3.158(30)	0.0034(27)
	O	7	3.310	3.305(114)	0.0045(16)
$Ce_{0.90}Pd_{0.10}O_{2-\delta}$, ($S_0^2 = 0.829$, $E_0 = -7.836$ eV, R-factor $= 0.0876$)	O	4	1.910	1.983(14)	0.0017(19)
	Ce	4	3.030	3.191(38)	0.0044(21)
	O	7	3.310	3.352(58)	0.0011(80)
$Ce_{0.83}Pd_{0.17}O_{2-\delta}$ + 0.03PdO, ($S_0^2 = 0.826$, $E_0 = -0.617$ eV, R-factor $= 0.0295$)	O (fluorite and PdO)	4	1.910	2.018(9)	0.0019(6)
	Pd (PdO)	0.6	3.030	3.130(78)	0.0003(22)
	Ce (fluorite)	3.4	3.030	3.192(44)	0.0044
	O (fluorite)	5.95	3.310	3.554(45)	0.0010
	Pd (PdO)	1.2	3.420	3.503(47)	0.0042(66)

This journal is © The Royal Society of Chemistry 2015

J. Mater. Chem. A, 2015, 3, 13072–13079 | **13075**

Fig. 5 *In situ* powder XRD patterns of $Ce_{1-x}Pd_xO_{2-\delta}$ ($x = 0.05, 0.10$ and 0.15) at 30 °C, 750 °C and 800 °C. Asterisks denote the position of peaks attributed to the sample holder.

powder XRD of $Ce_{0.70}Pd_{0.30}O_{2-\delta}$ shows the presence of nanocrystalline PdO as a secondary phase; and between $0.15 \leq x \leq 0.25$ the lattice parameter no longer increases linearly as a function of x (Fig. 2b), it is conceivable that a small amount of PdO, undetectable by powder XRD, is present as a second phase at $x = 0.20$. A two-phase model is difficult to fit to the EXAFS signal, however, since the Pd–Pd distance in PdO and the Pd–Ce distance in the doped model are both close to 3 Å. Therefore, some parameters had to be fixed in order to obtain a satisfactory fit: S_0^2 was fixed at 0.826, the value found for PdO (and very close to the value for the doped model), and the Debye–Waller factor for the Ce shell was fixed at 0.0044 Å^2 (found for the doped model) and the value for the second O shell at 0.001 Å^2. The proportion of Pd present as PdO was estimated by fitting the lattice parameter of the fluorite to the extrapolated linear fit (fitted over the region $0 \leq x \leq 0.15$) to give value of $x = 0.17$. This means that approximately 15% of the Pd is present as PdO and 85% is found in $Ce_{0.83}Pd_{0.17}O_{2-\delta}$. Fitting this model to the EXAFS spectrum gives a good fit (R-factor = 0.0295, Table 1). The addition PdO in this material must be of too small a crystal size to be resolved in the powder XRD. This is then consistent with the maximum amount of Pd in $Ce_{1-x}Pd_xO_{2-\delta}$ being $x = 0.15$ from our hydrothermal synthesis method.

Thermal stability and redox properties

In situ powder diffraction on heating in air of $Ce_{1-x}Pd_xO_{2-\delta}$ ($x = 0.05, 0.10$) shows the materials are stable up to at least 800 °C (Fig. 5), with no trace of Pd or PdO observed. However, although $Ce_{0.85}Pd_{0.15}O_{2-\delta}$ was observed to have only fluorite reflections at 750 °C, at 800 °C Pd metal peaks are also present, suggesting that at high Pd-content the oxide is less stable (Fig. 5).

H_2-TPR profiles of $Ce_{1-x}Pd_xO_{2-\delta}$ ($0 \leq x \leq 0.25$) up to 250 °C (Fig. 6a) show in each case the presence of a large, sharp, low

temperature reduction peak, which cannot be solely attributed to the reduction of Pd^{2+} to Pd metal on the basis of quantification of the amount of hydrogen consumed. The temperature of the maximum hydrogen uptake decreases as x increases, and the total amount of hydrogen oxidised tends to increase linearly with increasing x up to $x = 0.20$ (Fig. 6b). The TPR profile of hydrothermally prepared CeO_2 over the same range (not shown) showed no visible hydrogen oxidation. The increasing hydrogen oxidation in the Pd-containing materials cannot be solely attributed to the increasing amount of Pd^{2+} present being reduced: a significant, increasing proportion of Ce^{4+} reduction must be occurring (up to $x = 0.20$). Assuming complete

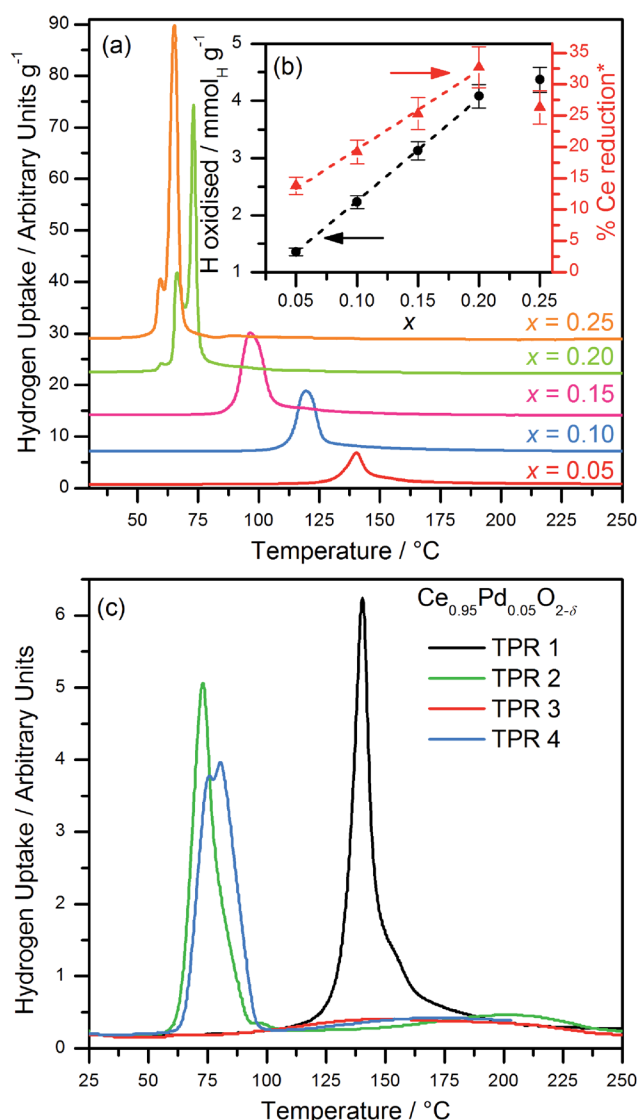**Fig. 6** (a) H_2-TPR profiles of $Ce_{1-x}Pd_xO_{2-\delta}$ ($0.05 \leq x \leq 0.25$, nominal compositions) from ambient temperature to 250 °C. (b) H oxidised per gram of sample and corresponding %Ce reduction as a function of x (* %Ce reduction, assuming complete Pd^{2+} reduction), with linear fit over range $0.05 \leq x \leq 0.20$. Error bars ±5%. (c) Cycled TPR experiments: TPR1 was performed on a freshly made sample, TPR2 after reoxidation at 700 °C, TPR3 after reoxidation at 500 °C and TPR4 after reoxidation to 700 °C.
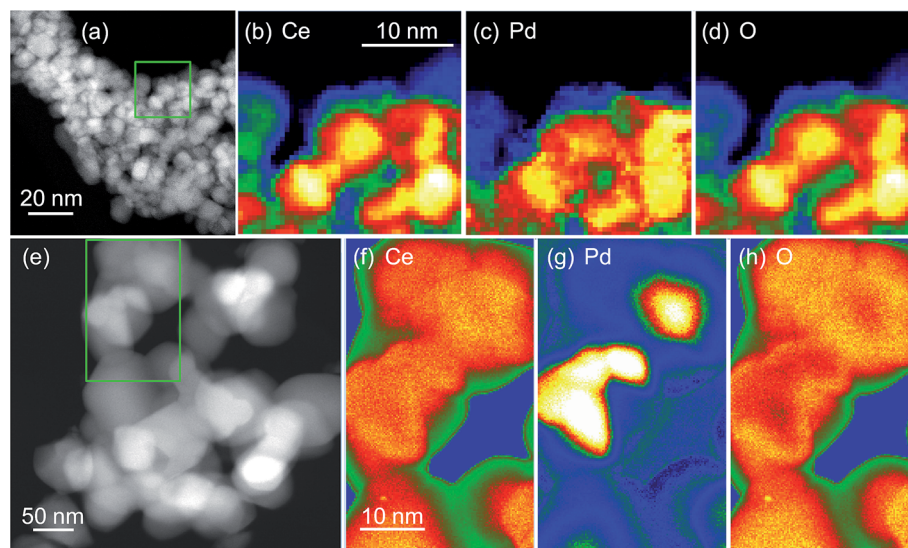
Fig. 7 HAADF images of crystallites in 5 mol% Pd–CeO$_2$ (a) before and (e) after heating oxidation in air at 800 °C and Ce M$_{4,5}$, Pd M$_{4,5}$ and O K EELS maps (b–d) before and (f–h) after oxidation. The green boxes in (a) and (e) show the areas selected for the EELS maps.

reduction of the Pd, then the percentage of cerium that is reduced can be calculated: this is plotted in Fig. 6b and the results shown in Table S3 of the ESI.† When $x \geq 0.20$ the reduction peak begins to split into two peaks, possibly due to the presence of a PdO impurity (as observed in the EXAFS analysis). The increasing proportion of Ce^{4+} reduction (up to $x = 0.20$) suggests that the presence of ionic Pd^{2+} distributed throughout the structure leads to greater reducibility of the Ce^{4+}. The origin of the enhanced reducibility of the materials can thus be ascribed to be due to a combination of the expansion of the lattice and the higher level of oxide defects as more Ce^{4+} is substituted by Pd^{2+}, both of which can be envisaged to enhance oxide-ion migration, in turn leading to more easy removal of oxygen with increased Pd content. Since the analysis above showed that further addition of Pd (i.e. intended $x = 0.25$) leads to the formation of amorphous PdO in an inhomogeneous mixture this explains the fact that this material has a lower than expected hydrogen uptake.

For the lowest concentration of Pd (5 mol%), the effect of recycling the TPR experiment was investigated, Fig. 6c. This shows that after re-oxidation to 700 °C the hydrogen reduction occurs at markedly lower temperature (~75 °C). This is reproducible (see TPR4 on Fig. 6c) but re-oxidation at the lower temperature of 500 °C is not sufficient to regenerate the low temperature reduction (TPR3). The material thus formed after the first TPR-TPO cycle resembles Pd dispersed on CeO$_2$: for example Luo et al. studied ceria onto which Pd had been added by wet impregnation and found the same sharp single reduction peak at 75 °C in the TPR.[35] The TPR trace of our Ce$_{0.95}$Pd$_{0.05}$O$_{1.95}$ material after a cycle of reduction–oxidation (TPR2 on Fig. 6c) is remarkably similar to that reported for Luo et al. for 2% and 5% Pd loaded on ceria. This would be consistent with the extrusion of Pd from the Pd-doped CeO$_2$ in the first TPR cycle in our materials to give surface Pd, suggesting an inherent instability of Pd when incorporated into the ceria lattice.

TEM before and after heat treatment, Fig. 7, confirms that Pd metal is easily released from the materials. The EELS maps clearly show how Pd is evenly dispersed in the same region as cerium in the as-made materials (Ce$_{0.95}$Pd$_{0.05}$O$_{2-\delta}$ in this case), but after heating in air the Pd is phase separated and agglomerates in separate particles, >10 nm in dimension. This would explain the results of TPR-TPO cycling where after reoxidising in air to 700 °C the materials resemble Pd dispersed on a CeO$_2$ support.

Experimental

Samples of Ce$_{1-x}$Pd$_x$O$_{2-\delta}$ (nominally $0 \leq x \leq 0.25$ in increments of $x = 0.05$) were prepared by hydrothermal reactions at 240 °C. CeCl$_3 \cdot$7H$_2$O (Aldrich, 99.9%) and PdCl$_2$ (Johnson Matthey, 99.8%) were mixed in a $(1 - x) : x$ molar ratio; respectively; to give a total of 6 mmol of metal ions. To this 2 ml cold H$_2$O was added, yielding a solution, to which 2 ml of H$_2$O$_2$ (Aldrich, 30% aqueous solution) was added. This mixture was stirred for 15 minutes before 8 ml of 7.5 M NaOH was added dropwise with effervescence. The red-brown gel was stirred for a further 10–15 minutes before being sealed in a Teflon-lined steel autoclave and placed in a pre-heated fan oven to 240 °C for 24 hours. The autoclave was cooled to room temperature before filtration and washing with copious amounts of boiling water. The resulting brown solids were dried in an oven at 80 °C overnight and ground in a pestle and mortar to give fine powders.

Powder X-ray diffraction (XRD) patterns for phase identification were measured using a Siemens D5000 diffractometer operating with Cu K$\alpha_{1/2}$ radiation. High resolution powder XRD data were collected using a Panalytical X'Pert Pro MPD diffractometer with monochromatic Cu Kα_1 radiation and a PIXcel solid-state detector. Non-ambient powder XRD measurements were made using a Bruker D8 Advance diffractometer with Cu

This journal is © The Royal Society of Chemistry 2015

J. Mater. Chem. A, 2015, 3, 13072–13079 | **13077**

$K\alpha_{1/2}$ radiation and fitted with a VÅNTEC-1 high-speed detector. Powders were heated *in situ* using an Anton Paar XRK 900 reaction chamber controlled either in static air or under a flow of 5% hydrogen in nitrogen. Powder XRD patterns were fitted using a Le Bail profile refinement with the GSAS software,[36] which allowed refinement of lattice parameters and peak broadening parameters.

Thermogravimetric analysis (TGA) was performed using a Mettler Toledo Systems TGA/DSC 1 instrument under an air flow of 50 ml min^{-1} from room temperature to 1000 °C at a heating rate of 10 °C min^{-1}.

Inductively coupled plasma optical emission spectroscopy (ICP-OES) was used to determine the amounts of the metals present in the samples by the company MEDAC Ltd (UK).

XANES and EXAFS spectra were measured using B18 at Diamond Light Source.[37] Data were collected in transmission mode at the Ce L$_{III}$-edge and the Pd K-edge from samples diluted with appropriate amounts of polyethylene powder and pressed in self-supporting discs around 1 mm thick. The incident energy was selected using a water-cooled, fixed-exit, double-crystal monochromator with Si (311) crystals. On B18 a double toroidal mirror, coated with Cr and Pt, 25 m from the source is used to focus the beam horizontally and vertically onto the sample and a pair of smaller plane mirrors are used for harmonic rejection. The raw data were treated using the programme Athena[38] to produce XANES spectra, normalised to the post-edge background, and normalised EXAFS spectra. The Pd K-edge EXAFS spectra were analysed using the software Artemis,[38] which implements the FEFF code, over the k-range 3–12 Å^{-1}. For the crystalline reference material PdO the coordination numbers were set at values expected from the known structure and shell distances (R) and thermal parameters (σ^2) along with threshold energy (E_0) and amplitude reduction factor (S_0^2) were allowed to vary in least-squares refinements to obtain a satisfactory fit to the k^3-weighted EXAFS. For the Pd-containing ceria samples, various structural models were considered, as described below, and the goodness of fit assessed, while it was checked that the refined amplitude reduction factor (S_0^2) gave a value similar to that obtained for PdO.

High resolution transmission electron microscopy (TEM) and electron energy loss spectrum imaging (EELS-SI) studies were performed on a probe-corrected JEOL ARM 200F microscope operating at 200 kV and equipped with a Gatan GIF Quantum ER spectrometer. High angle annular dark field (HAADF) images were produced and for EELS-SI a dispersion of 0.5 eV per channel was set and spectra with 2048 channels were recorded with an energy range of 1024 eV in each spectrum. The Gatan spectrum imaging plugin was used for EELS-SI acquisitions. This yielded 3D data sets with each pixel containing an individual EELS spectrum. Elemental maps of Pd M$_{4,5}$-edge, O K-edge, and Ce M$_{4,5}$-edge were produced after a suitable pre-edge inverse power law background fitting with energy windows of 30 eV, 35 eV, and 45 eV respectively. Temperature programmed reduction (TPR) was measured by thermal conductivity of the 10% H$_2$ in N$_2$ (at a flow rate of 30 ml min^{-1}) before and after contact with the 0.05–0.10 g sample. A H$_2$O trap after the sample was used to absorb water created by H$_2$ oxidation.

Temperature was increased linearly as a function of time. In order to quantify accurately the hydrogen consumption a known quantity (1 ml) of N$_2$ was injected into the H$_2$/N$_2$ gas stream before the experiment began to create a calibration peak. Quantification of H$_2$ consumption was carried by the integration of TPR profile as a function of time. Results are presented as the amount of H atoms oxidised per gram of sample, mmol (H) g^{-1}. The error is estimated to be ±5% for the total H$_2$ consumption in these measurements. Temperature programme oxidation (TPO) in the same apparatus was performed with 10% O$_2$ in He at the same flow rate to examine recyclability of the materials.

Conclusions

In conclusion, a series of nanocrystalline Pd-substituted ceria-type fluorites of the form Ce$_{1-x}$Pd$_x$O$_{2-\delta}$ ($0.05 \le x \le 0.15$) have been prepared by low-temperature hydrothermal synthesis. Attempts to achieve a higher value of Pd substitution led to the formation of PdO as a secondary phase. Analysis of the Pd K-edge EXAFS and the powder XRD have been used to infer a square-planar coordination, brought about by Pd offset from the Ce sites within the fluorite structure and also giving under-coordinated oxide ions and oxide vacancies. This supports a previously proposed model from computer simulation. The oxides have been demonstrated by *in situ* powder XRD to be stable in air up to at least 750–800 °C, but that Pd is extruded from the materials on heating beyond this. H$_2$-TPR shows that increasing the Pd substitution leads to improved low-temperature reducibility of the oxides, but that on cycling the materials resemble Pd dispersed on ceria, consistent with an inherent instability of Pd^{2+} within the ceria lattice. Despite this, the material formed has a reduction profile that resembles Pd dispersed onto pre-made ceria by we impregnation, and so a material with potential use in catalysis is formed. Further work would be required to understand the structural distortions introduced by Pd^{2+} in ceria, such as by pair distribution function analysis, and also it would be informative to perform an *in operando* spectroscopic study to analyse the migration of Pd from the lattice to the surface of ceria, as this would allow the mechanism of redox chemistry to be understood.

Acknowledgements

References

1 H. Kušar, S. Hočevar and J. Levec, *Appl. Catal., B*, 2006, **63**, 194; A. Trovarelli and P. Fornasiero, *Catalysis by Ceria and Related Materials*, Imperial College Press, London, 2nd edn, 2013.

2 A. Trovarelli, *Catal. Rev.: Sci. Eng.*, 1996, **38**, 439.

3 F. Giordano, A. Trovarelli, C. de Leitenburg and M. Giona, *J. Catal.*, 2000, **193**, 273.

4 P. Fornasiero, R. Di Monte, G. R. Rao, J. Kašpar, S. Meriani, A. Trovarelli and M. Graziani, *J. Catal.*, 1995, **151**, 168; D. Martin and D. Duprez, *J. Phys. Chem.*, 1996, **100**, 9429; Y. Liu, T. Hayakawa, T. Ishii, M. Kumagai, H. Yasuda, K. Suzuki, S. Hamakawa and K. Murata, *Appl. Catal., A*, 2001, **210**, 301; N. Barrabés, K. Föttinger, A. Dafinov, F. Medina, G. Rupprechter, J. Llorca and J. E. Sueiras, *Appl. Catal., B*, 2009, **87**, 84.

5 J. Kašpar, P. Fornasiero and M. Graziani, *Catal. Today*, 1999, **50**, 285; R. Di Monte and J. Kašpar, *Top. Catal.*, 2004, **28**, 47.

6 R. J. Gorte, *AIChE J.*, 2010, **56**, 1126.

7 S. Hilaire, X. Wang, T. Luo, R. J. Gorte and J. Wagner, *Appl. Catal., A*, 2001, **215**, 271.

8 A. T. Bell, *Science*, 2003, **299**, 1688; P. Fornasiero, G. Balducci, J. Kašpar, S. Meriani, R. Di Monte and M. Graziani, *Catal. Today*, 1996, **29**, 47.

9 R. Di Monte and J. Kašpar, *J. Mater. Chem.*, 2005, **15**, 633.

10 M. Cargnello, J. J. Delgado Jaen, J. C. Hernandez Garrido, K. Bakhmutsky, T. Montini, J. J. Calvino Gamez, R. J. Gorte and P. Fornasiero, *Science*, 2012, **337**, 713; S. Colussi, A. Gayen, M. F. Camellone, M. Boaro, J. Llorca, S. Fabris and A. Trovarelli, *Angew. Chem., Int. Ed.*, 2009, **48**, 8481.

11 G. Ranga Rao and B. G. Mishra, *Bull. Catal. Soc.*, 2003, **2**, 122.

12 J. A. Kurzman, L. M. Misch and R. Seshadri, *Dalton Trans.*, 2013, 14653.

13 T. Baidya, A. Gayen, M. S. Hegde, N. Ravishankar and L. Dupont, *J. Phys. Chem. B*, 2006, **110**, 5262; T. Baidya, M. S. Hegde and J. Gopalakrishnan, *J. Phys. Chem. B*, 2007, **111**, 5149.

14 W. Huang, P. Shuk and M. Greenblatt, *Chem. Mater.*, 1997, **9**, 2240; H. L. Tuller and A. S. Nowick, *J. Electrochem. Soc.*, 1975, **122**, 255; B. C. H. Steele, *Solid State Ionics*, 2000, **129**, 95.

15 G. B. Balazs and R. S. Glass, *Solid State Ionics*, 1995, **76**, 155.

16 M. S. Hegde, G. Madras and K. C. Patil, *Acc. Chem. Res.*, 2009, **42**, 704.

17 A. Gayen, K. R. Priolkar, P. R. Sarode, V. Jayaram, M. S. Hegde, G. N. Subbanna and S. Emura, *Chem. Mater.*, 2004, **16**, 2317; A. R. Derk, G. M. Moore, S. Sharma, E. W. McFarland and H. Metiu, *Top. Catal.*, 2014, **57**, 118.

18 K. R. Priolkar, P. Bera, P. R. Sarode, M. S. Hegde, S. Emura, R. Kumashiro and N. P. Lalla, *Chem. Mater.*, 2002, **14**, 2120.

19 P. Bera, K. C. Patil, V. Jayaram, G. N. Subbanna and M. S. Hegde, *J. Catal.*, 2000, **196**, 293.

20 P. Singh and M. S. Hegde, *Cryst. Growth Des.*, 2010, **10**, 2995.

21 L. M. Misch, J. A. Kurzman, A. R. Derk, Y.-I. Kim, R. Seshadri, H. Metiu, E. W. McFarland and G. D. Stucky, *Chem. Mater.*, 2011, **23**, 5432.

22 M. Kurnatowska, L. Kepinski and W. Mista, *Appl. Catal., B*, 2012, **117–118**, 135.

23 P. Singh and M. S. Hegde, *Chem. Mater.*, 2009, **21**, 3337.

24 R. I. Walton, *Prog. Cryst. Growth Charact. Mater.*, 2011, **57**, 93.

25 R. Mistri, J. Llorca, B. C. Ray and A. Gayen, *J. Mol. Catal. A: Chem.*, 2013, **376**, 111.

26 D. O. Scanlon, B. J. Morgan and G. W. Watson, *Phys. Chem. Chem. Phys.*, 2011, **13**, 4279.

27 T. Baidya, G. Dutta, M. S. Hegde and U. V. Waghmare, *Dalton Trans.*, 2009, **3**, 455; S. Sharma, Z. Hu, P. Zhang, E. W. McFarland and H. Metiu, *J. Catal.*, 2011, **278**, 297; L. Meng, A.-P. Jia, J.-Q. Lu, L.-F. Luo, W.-X. Huang and M.-F. Luo, *J. Phys. Chem. C*, 2011, **115**, 19789.

28 A. Gupta, M. S. Hegde, K. R. Priolkar, U. V. Waghmare, P. R. Sarode and S. Emura, *Chem. Mater.*, 2009, **21**, 5836; A. Gupta, A. Kumar, U. V. Waghmare and M. S. Hegde, *Chem. Mater.*, 2009, **21**, 4880.

29 R. D. Shannon, *Acta Crystallogr., Sect. A: Cryst. Phys., Diffr., Theor. Gen. Crystallogr.*, 1976, **32**, 751.

30 J. Waser, H. A. Levy and S. W. Peterson, *Acta Crystallogr., Sect. A: Cryst. Phys., Diffr., Theor. Gen. Crystallogr.*, 1953, **6**, 661.

31 J. P. Attfield, *Acta Crystallogr., Sect. B: Struct. Sci.*, 1988, **44**, 563.

32 K. Sardar, H. Y. Playford, R. J. Darton, E. R. Barney, A. C. Hannon, D. Tompsett, J. Fisher, R. J. Kashtiban, J. Sloan, S. Ramos, G. Cibin and R. I. Walton, *Chem. Mater.*, 2010, **22**, 6191; G. Li, R. L. Smith and H. Inomata, *J. Am. Chem. Soc.*, 2001, **123**, 11091.

33 P. Nachimuthu, W. C. Shih, R. S. Liu, L. Y. Jang and J. M. Chen, *J. Solid State Chem.*, 2000, **149**, 408.

34 T. Baidya, K. R. Priolkar, P. R. Sarode, M. S. Hegde, K. Asakura, G. Tateno and Y. Koike, *J. Chem. Phys.*, 2008, **128**, 124711.

35 M. F. Luo, Z. Y. Hou, X. X. Yuan and X. M. Zheng, *Catal. Lett.*, 1998, **50**, 205.

36 A. C. Larson and R. B. Van Dreele, Los Alamos National Laboratory Report LAUR, 1994, 86.

37 A. J. Dent, G. Cibin, S. Ramos, A. D. Smith, S. M. Scott, L. Varandas, M. R. Pearson, N. A. Krumpa, C. P. Jones and P. E. Robbins, *J. Phys.: Conf. Ser.*, 2009, **190**, 012039.

38 B. Ravel and M. Newville, *J. Synchrotron Radiat.*, 2005, **12**, 537.

This journal is © The Royal Society of Chemistry 2015

J. Mater. Chem. A, 2015, **3**, 13072–13079 | **13079**